Since January 2020 Elsevier has created a COVID-19 resource centre with free information in English and Mandarin on the novel coronavirus COVID-19. The COVID-19 resource centre is hosted on Elsevier Connect, the company's public news and information website.

Cell Reports

Monoclonal antibodies protect aged rhesus macaques from SARS-CoV-2-induced immune activation and neuroinflammation

Graphical abstract

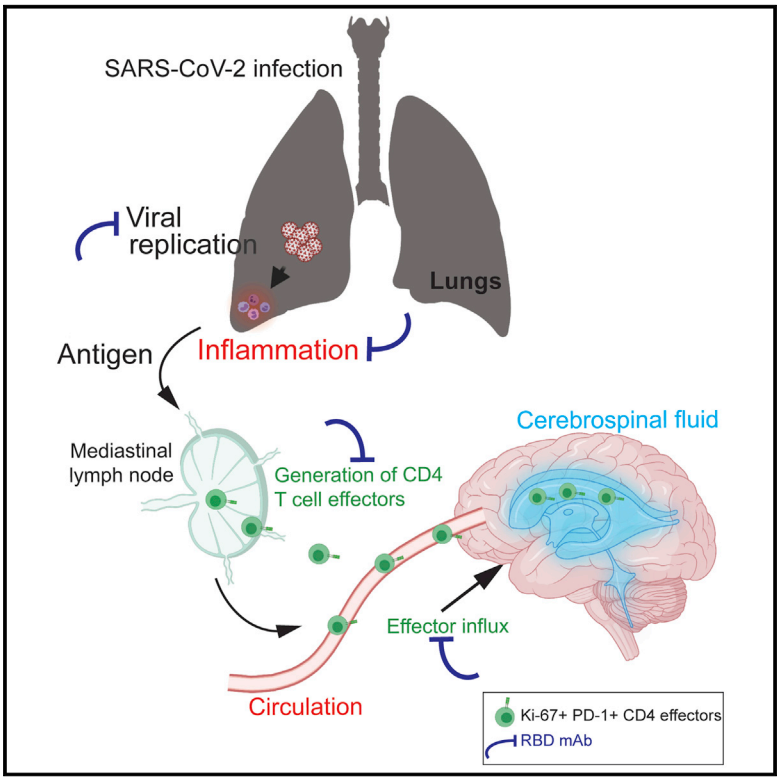

Highlights

- Neutralizing monoclonal antibodies (mAbs) block SARS-CoV-2 replication
- Neutralizing mAbs prevent SARS-CoV-2-induced interferon-induced chemokines
- Neutralizing mAbs limit effector CD4 T cell influx into cerebrospinal fluid

Authors

Anil Verma, Chase E. Hawes, Yashavanth Shaan Lakshmanappa, ..., Koen K.A. Van Rompay, John H. Morrison, Smita S. Iyer

Correspondence

smiyer@ucdavis.edu

In brief

Verma et al. observe that prophylactic mAbs limit SARS-CoV-2 replication and immune activation. In aged diabetic rhesus macaques, these protective mechanisms took place in the areas of the body most highly targeted by the virus and the respiratory, nervous, and circulatory systems.

Verma et al., 2021, Cell Reports *37*, 109942
November 2, 2021
https://doi.org/10.1016/j.celrep.2021.109942

Cell Reports

CellPress
OPEN ACCESS

Report

Monoclonal antibodies protect aged rhesus macaques from SARS-CoV-2-induced immune activation and neuroinflammation

Anil Verma,[1] Chase E. Hawes,[1,2] Yashavanth Shaan Lakshmanappa,[1] Jamin W. Roh,[1,2] Brian A. Schmidt,[1] Joseph Dutra,[3] William Louie,[4] Hongwei Liu,[4] Zhong-Min Ma,[3] Jennifer K. Watanabe,[3] Jodie L. Usachenko,[3] Ramya Immareddy,[3] Rebecca L. Sammak,[3] Rachel Pollard,[3] J. Rachel Reader,[3,4] Katherine J. Olstad,[3,4] Lark L. Coffey,[4] Pamela A. Kozlowski,[5] Dennis J. Hartigan-O'Connor,[3,6] Michel Nussenzweig,[7] Koen K.A. Van Rompay,[3,4] John H. Morrison,[3,8,9] and Smita S. Iyer[1,3,4,9,10,*]

[1]Center for Immunology and Infectious Diseases, University of California, Davis, Davis, CA 95616, USA
[2]Graduate Group in Immunology, University of California, Davis, Davis, CA 95616, USA
[3]California National Primate Research Center, University of California, Davis, Davis, CA 95616, USA
[4]Department of Pathology, Microbiology, and Immunology, School of Veterinary Medicine, University of California, Davis, Davis, CA 95616, USA
[5]Department of Microbiology, Immunology, and Parasitology, Louisiana State University Health Sciences Center, New Orleans, LA 70112, USA
[6]Department of Medical Microbiology and Immunology, School of Medicine, University of California, Davis, Davis, CA 95616, USA
[7]Laboratory of Molecular Immunology, The Rockefeller University, New York, NY 10065, USA
[8]Department of Neurology, School of Medicine, University of California, Davis, Davis, CA 95616, USA
[9]Senior author
[10]Lead contact
*Correspondence: smiyer@ucdavis.edu
https://doi.org/10.1016/j.celrep.2021.109942

SUMMARY

Anti-viral monoclonal antibody (mAb) treatments may provide immediate but short-term immunity from coronavirus disease 2019 (COVID-19) in high-risk populations, such as people with diabetes and the elderly; however, data on their efficacy in these populations are limited. We demonstrate that prophylactic mAb treatment blocks viral replication in both the upper and lower respiratory tracts in aged, type 2 diabetic rhesus macaques. mAb infusion dramatically curtails severe acute respiratory syndrome coronavirus 2 (SARS-CoV-2)-mediated stimulation of interferon-induced chemokines and T cell activation, significantly reducing development of interstitial pneumonia. Furthermore, mAb infusion significantly dampens the greater than 3-fold increase in SARS-CoV-2-induced effector CD4 T cell influx into the cerebrospinal fluid. Our data show that neutralizing mAbs administered preventatively to high-risk populations may mitigate the adverse inflammatory consequences of SARS-CoV-2 exposure.

INTRODUCTION

Effective deployment of multiple severe acute respiratory syndrome coronavirus 2 (SARS-CoV-2) vaccines combined with aggressive vaccination campaigns have led to marked reductions in severe disease, hospitalizations, and death, including those caused by the variants of concern (Haas et al., 2021; Hall et al., 2021; Moghadas et al., 2020). However, vaccine hesitancy, lagging vaccine coverage in low- to middle-income countries, impaired vaccine-induced immunity in the immunosuppressed, and the threat of severe viral variants continue to complicate the rates of morbidity and mortality attributed to SARS-CoV-2 infection (Dror et al., 2020; Raja et al., 2021; Mathieu et al., 2021; Thakkar et al., 2021). Consequently, passive immunization using anti-viral monoclonal antibody (mAb) treatments may be an important tool for preventing breakthrough infections and mitigating immunopathological manifestations of coronavirus disease 2019 (COVID-19) in high-risk populations (Cohen et al., 2021).

Multiple studies have demonstrated that mAbs targeting the receptor-binding domain (RBD) of the SARS-CoV-2 spike accelerate viral clearance in both preventative and therapeutic settings in rhesus models of COVID-19 (Baum et al., 2020; Shi et al., 2020; Zost et al., 2020; Kim et al., 2021). However, the efficacy of these mAbs in preventing viral establishment and replication in aged rhesus macaques with comorbidities is unknown, and information on the subsequent innate and adaptive immune response, particularly within the cerebrospinal fluid (CSF), in SARS-CoV-2 infections is minimal (Channappanavar and Perlman, 2020). Bridging this gap is important in understanding the extent to which mAb-based interventions limit virus replication

and inflammatory consequences of antigen exposure in high-risk patients.

In this study, we evaluated the prophylactic efficacy of two highly potent human mAbs, C135-LS and C144-LS, which carry half-life extension mutations and target non-overlapping epitopes of the spike protein (Robbiani et al., 2020), in protecting aged rhesus macaques from SARS-CoV-2 infection and associated immune activation. We previously found these antibodies to have therapeutic benefits when given to macaques 1 day after SARS-CoV-2 inoculation (Van Rompay et al., 2021). Our current data demonstrate that a mAb cocktail infused 3 days prior to virus inoculation blocked active viral replication with dramatic effects in the upper and lower respiratory tracts. Although activation of inflammatory pathways was still observed, mAb therapy curtailed infection-induced T cell activation, resulting in reduced T cells in cell cycle within the effector-permissive CSF compartment. Our data in aged macaques with comorbidities provide an important proof of concept that prophylactic mAb treatment of SARS-CoV-2 limits immune activation in distinct tissue compartments impacted by SARS-CoV-2.

RESULTS AND DISCUSSION

mAbs block SARS-CoV-2 replication in the upper respiratory tract, limit interstitial pneumonia, and prevent T cell activation

To determine the degree to which mAb therapy prevents infection and immune activation in high-risk populations, we infused four immunocompetent, aged, type 2 diabetic rhesus macaques (21–22 years of age, corresponding to 63–66 years in humans; Table S1; Figure 1A) with a combination of two mAbs, C135-LS and C144-LS, that target distinct regions of the spike RBD (Robbiani et al., 2020). Each RBD mAb was dosed at 20 mg/kg, and the cocktail was administered 3 days prior to viral challenge to allow for maximal tissue penetration in the respiratory tract. Animals in the control group (18–23 years) were infused with a control non-specific mAb (3BNC117 anti-HIV mAb). Animals in both groups were hypertensive (n = 2 in control group; n = 1 in RBD mAb group) and were on medications for a variety of chronic conditions, reflective of comorbidities in the aged human population (Table S2). All animals were inoculated intranasally and intratracheally with SARS-CoV-2 at a high dose (2.5×10^6 plaque-forming units [PFUs]), a dose and challenge stock that resulted in infection of 100% of macaques after a single challenge in our previous studies (Shaan Lakshmanappa et al., 2021; Van Rompay et al., 2021) and those by other investigators (Chandrashekar et al., 2020; Chang et al., 2021; Singh et al., 2021). Animals were euthanized 7 days later to capture the peak of the effector T cell response (Figure 1A). Samples from the upper and lower respiratory tracts, CSF, and blood were collected to assess viral and inflammatory dynamics in distinct tissue compartments. Samples were taken at 3 and 7 days post-challenge to minimize sedation-related physiological distress in aged animals.

Post-mAb infusion, all animals exhibited robust neutralizing activity in sera with neutralizing titer (NT_{50}: reciprocal dilution of sera required to inhibit viral replication by 50%) >10,000 at day of inoculation (range: 12,738–56,374) with a gradual decay from day 0 to day 7 (range: 4,198–24,977) (Figure 1B).

Clinical signs of infection were generally mild and did not require intervention (Figure S1A). Upper respiratory symptoms, such as sneezing and nasal discharge, were seen in three of four control animals and none of the RBD mAb-treated animals. Increased respiratory effort was observed in half of the control animals and in one of four treated animals. One animal in the treated group developed clinical signs of partial gastrointestinal obstruction immediately prior to inoculation requiring fluid therapy before and during the study period, elevating the clinical score.

Only one animal in the control group had increased interstitial infiltrates on radiographs on days 3 and 7 post-infection. No changes were observed in radiographs of the treated animals. Overall, the animals did not develop marked respiratory or clinical symptoms or significant perturbations in serum clinical analytes during the 7 days post-SARS-CoV-2 exposure (Figure S1B).

To evaluate the ability of mAbs in preventing SARS-CoV-2 infection, we assessed subgenomic viral RNA (sgRNA), a marker for actively replicating virus, genomic RNA (gRNA; targeting ORF1a), and viral RNA (vRNA; targeting SARS nucleoprotein [N]) levels by quantitative real-time PCR (Dagotto et al., 2021) in nasal swabs and bronchoalveolar lavage fluid (BALF). The kinetics of sgRNA, gRNA, and vRNA were similar in controls, with vRNA peaking at day 3 and gradually declining by day 7 (Figures 1C and 1D). The complete absence of sgRNA in the RBD mAb group demonstrated protection against viral replication in the upper and lower respiratory tracts. Specifically, at days 3 and 7, vRNA levels were reduced by approximately 3 logs compared with controls. We assessed vRNA in lung lobes and found greater vRNA in the right caudal lobe relative to the left caudal lobe in controls, consistent with previous studies and supporting focal replication within the respiratory tract (Figure 1E). vRNA was detected within the left caudal lobe in one of four animals in the RBD mAb group compared with three of four control animals. Within the right caudal lobe, no RBD mAb-treated animals exhibited vRNA above the limit of detection (LOD), whereas all four control animals were positive.

Assessment of viral titers by plaque assay identified infectious virus in the lungs of three controls and none of the RBD mAb-treated animals (Figure 1F). vRNA levels in the draining mediastinal lymph node closely matched infectious titers in controls (Figure 1G). Together, the data show that RBD mAb infusion prevented viral replication in the nasal cavity. vRNA was observed in the lung and lymph node in two of the RBD mAb-infused animals possessing the lowest observed serum-neutralizing activity. The differences in vRNA in one of the control animals (C2) across the upper and lower airways could be because of variation in viral kinetics, an observation consistent with other studies (Singh et al., 2021; Chandrashekar et al., 2020) indicative of disparity in viral replication across the respiratory tract. Indeed, we also observed differential impact of mAb efficacy on viral replication in the airways versus the lung parenchyma, suggesting that tissue-specific factors and/or neutralizing activity may be variably regulated across the airways. Altogether, the data are in line with a recent study demonstrating that neutralizing mAb reduced

CellPress
OPEN ACCESS

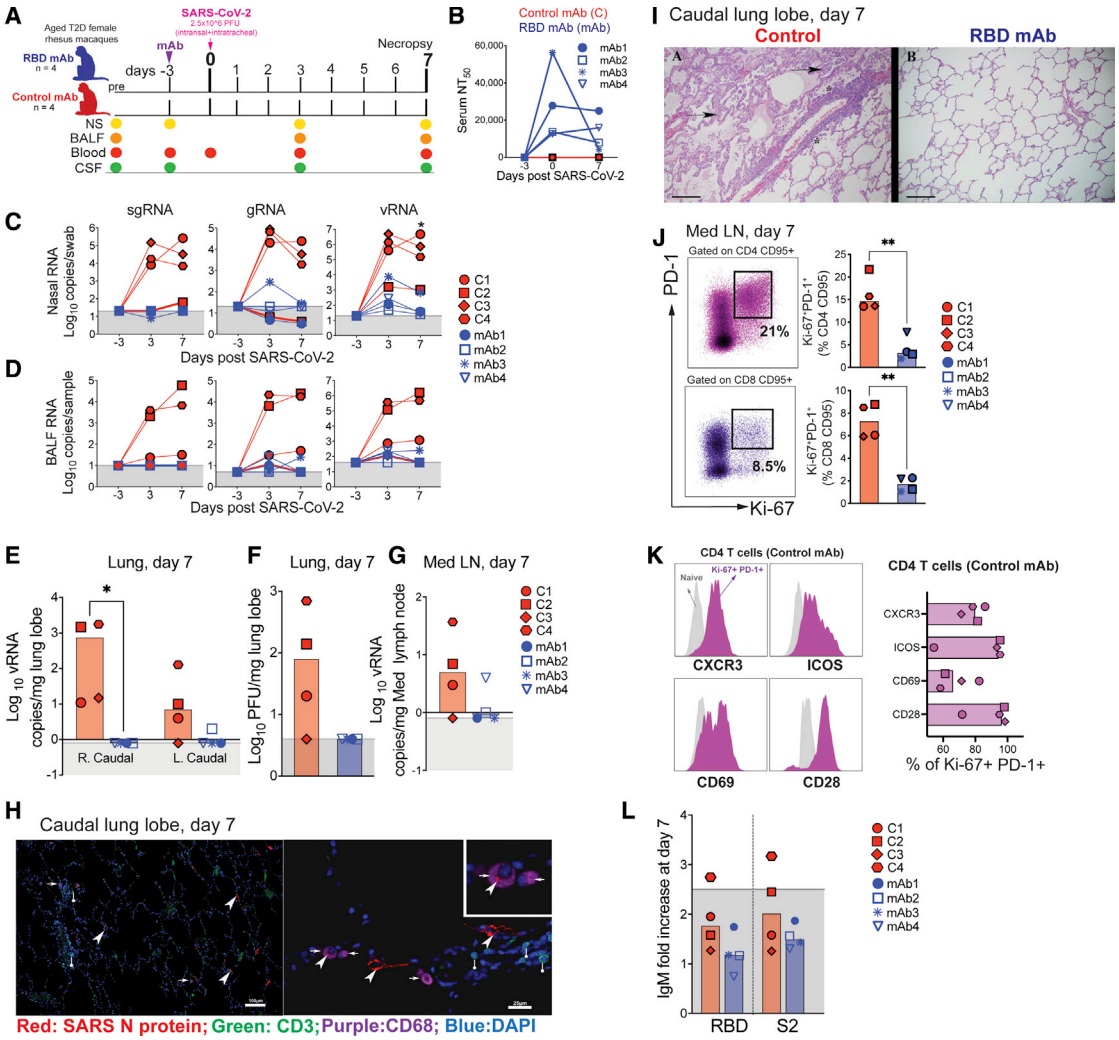

Figure 1. Monoclonal antibodies (mAbs) block SARS-CoV-2 replication in the upper respiratory tract, limit interstitial pneumonia, and prevent T cell activation

(A) Study schematic: rhesus macaques were infused intravenously (i.v.) with RBD-specific C135 and C144 mAb (RBD mAb, n = 4) or HIV-specific 3BNC117 mAb (control mAb [C], n = 4) 3 days prior to SARS-CoV-2 (2.5×10^6 PFUs) challenge. Nasal swabs (NSs), bronchoalveolar lavage (BAL) fluid (BALF), cerebrospinal fluid (CSF) taps, and blood collections were performed on indicated days. Necropsies were performed on day 7 post-SARS-CoV-2.

(B) Kinetics of serum neutralizing titer 50% (NT_{50}) determined by SARS-CoV-2 pseudotyped neutralization assay. Data shown are average of two independent technical replicates.

(C and D) Detection of SARS-CoV-2 subgenomic viral RNA (sgRNA), genomic RNA (gRNA), and viral RNA (vRNA) copies per NS (C) and BAL on indicated days during SARS-CoV-2 infection (D). Data in (C) and (D) are from single technical replicates.

(E and F) Quantification of vRNA copies in right or left caudal lobes (E) and PFUs per lobe from lung biopsy samples (F).

(G) Quantification of vRNA copies in mediastinal lymph nodes (Med LNs). Data in (E)–(G) are average of technical duplicates.

(H) Representative immunofluorescence staining of caudal lung lobes from a control mAb-treated animal. Large arrows denote SARS-CoV-2 N protein, small arrows denote $CD68^+$ pneumocytes, and ball/stick indicate $CD3^+$ T cells. Scale bar (left) 100μm; (right) 25μm

(I) Representative H&E images from the right caudal lung lobe harvested at necropsy, 7 days post-infection (pi) of (A) control mAb-treated animals illustrating region of moderately severe interstitial pneumonia (arrow) and perivascular inflammatory cell cuffing (asterisk). (B) RBD mAb-treated animals illustrating the lack of significant interstitial cellular infiltrates. Scale bar: 200 μm. An average of 16 H&E-stained sections of the right caudal lung lobe from all eight animals were examined for histological changes.

(J) Representative flow diagram identifying $Ki\text{-}67^+PD\text{-}1^+$ populations among $CD95^+$ CD4 and CD8 T cells (left) and their frequencies (right) in Med LNs.

(K) Median fluorescence intensity (left) or frequency (right) of naive or $Ki\text{-}67^+PD\text{-}1^+$ CD4 T cells expressing CXCR3, ICOS, CD69, or CD28 from day 7 Med LNs of control mAb-treated animals. Flow data represent a single technical replicate.

(L) Serum IgM against SARS-CoV-2 RBD and S2 from a single technical replicate.

Data points represent individual animals, with bars indicating medians. Gray bars indicate limit of detection (C–G and L). $^*p < 0.05$, $^{**}p < 0.01$, by two-tailed Mann-Whitney U test.

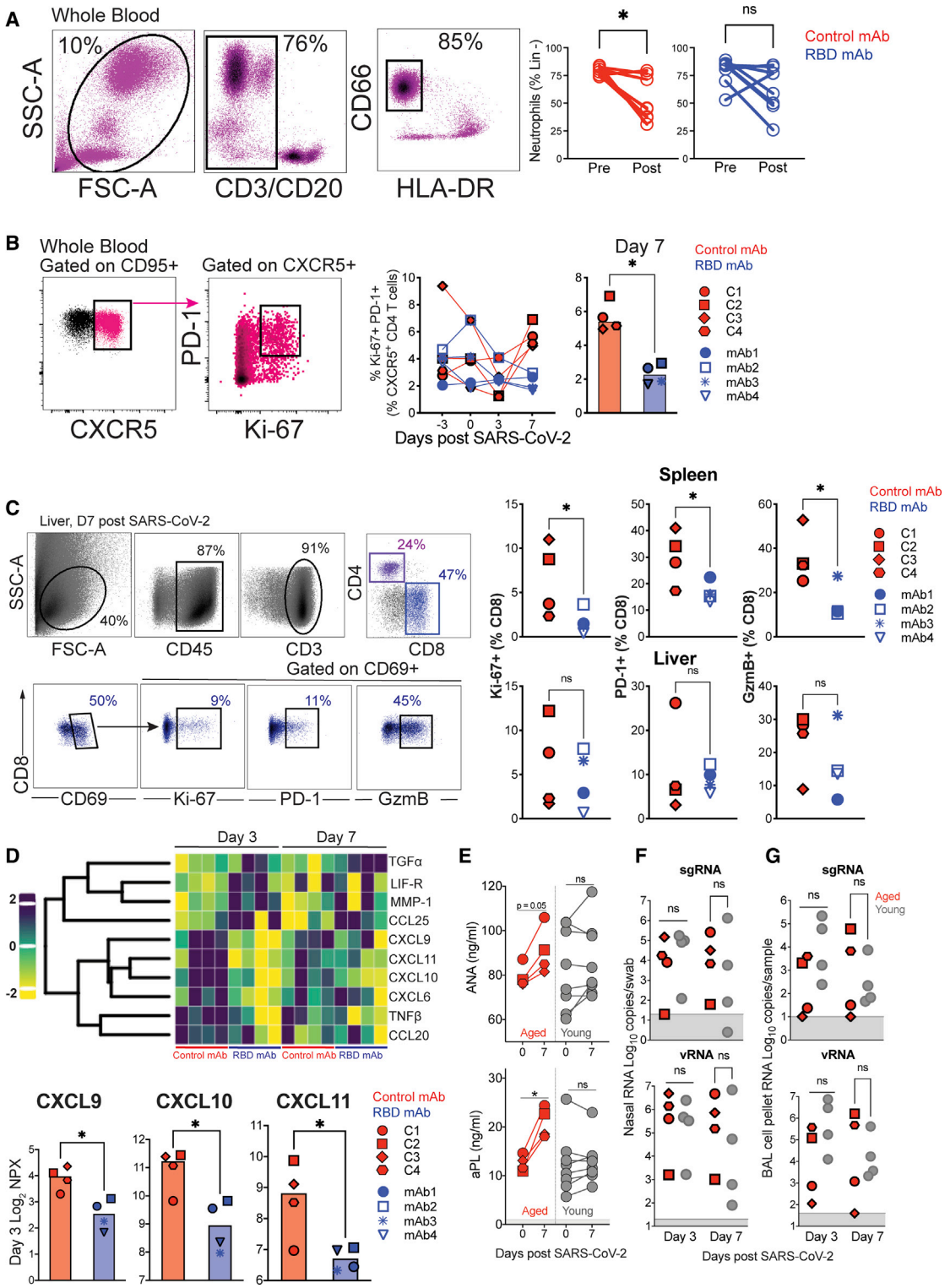

Figure 2. mAbs limit SARS-CoV-2-induced systemic immune activation

(A and B) Gating strategy and frequencies of (A) neutrophils ($CD3/20^{-}HLA\text{-}DR^{-}CD66^{+}$) at days −3 and 0 (pre) versus days 3 and 7 (post) and (B) $Ki\text{-}67^{+}PD\text{-}1^{+}$ T_{fh} cells ($CD95^{+}CXCR5^{+}$) in whole blood (n = 4 in each group).

(C) Gating strategy and frequency of $CD8^{+}CD69^{+}$ T cells expressing Ki-67, PD-1, or granzyme B (GzmB) in liver and spleen 7 days pi.

(legend continued on next page)

the incidence of COVID-19 in a nursing and assisted living facility (Cohen et al., 2021).

Consistent with quantitative real-time PCR and titration data, we detected N protein in the left caudal lobe in three of four controls, but not in the mAb-infused animals; N protein was largely colocalized with pneumocytes. Sporadic $CD3^+$ T cells in the lung were not colocalized with N protein (Figure 1H). In addition, we found a marked difference in histopathological lesions between the groups. The animals that received control mAb all had randomly scattered regions of interstitial pneumonia. In affected areas, alveolar septae were variably expanded by inflammatory cells often accompanied by perivascular cuffing of small- and medium-size blood vessels with mixed inflammation as previously described (Shaan Lakshmanappa et al., 2021). In three of four animals, the disease was considered moderate, while one animal had mild disease. The animals given the RBD mAb treatment had minimal to no evidence of interstitial pneumonia. The visual difference between the groups was striking and readily apparent without further semiquantitative scoring, indicating that RBD mAb treatment prior to SARS-CoV-2 infection prevents the development of any significant interstitial pneumonia (Figure 1I).

To identify immune activation in the lower respiratory tract, we analyzed inflammatory biomarkers in serially sampled cell-free BALF. A principal-component analysis (PCA) showed segregation of inflammatory proteins across treatment groups at day 3. This distribution was largely driven by six proteins (Figure S1C). A protein associated with severe lung damage in COVID-19, monocyte chemotactic protein (MCP-3) (Yang et al., 2020), responsible for directing monocyte recruitment to inflammatory sites, was significantly reduced in RBD mAb-treated animals relative to controls at day 7. BALF analysis revealed that concentrations of oncostatin M (OSM), a member of the IL-6 cytokine family, significantly increased at day 7 post-SARS-CoV-2 infection with no distinct treatment effects.

In further support of the efficacy of mAb in restricting viral replication, T cell activation in draining mediastinal lymph nodes, evidenced by co-expression of Ki-67 and PD-1, decreased 4-fold in the mAb group (Figure 1J). Phenotyping of the effectors in the control group showed that CD4 effectors expressing the T helper 1 (Th1) chemokine receptor CXCR3 were positive for the inducible T cell co-stimulator (ICOS), continued to express CD28, and were $CD69^+$, indicating recent activation, which is consistent with our previous observations (Shaan Lakshmanappa et al., 2021) (Figure 1K). Assessment of antibody responses to spike and N proteins revealed no evidence of seroconversion in the mAb group. One animal in the control group presented with >2.5-fold increases in anti-RBD and anti-S2 IgM, reflecting early production of antibody, consistent with the day 7 time point studied (Figure 1L). These data reinforce the importance of mAb treatment in restricting viral replication. Because the greatest impact is observed in the upper respiratory tract, mAb therapy could significantly curb viral shedding and transmission.

mAbs limit SARS-CoV-2-induced systemic immune activation

To evaluate whether immune activation in the lung resulted in dynamic changes to the systemic immune compartment, we assessed immune subsets that were transiently regulated following SARS-CoV-2 infection as we previously reported (Shaan Lakshmanappa et al., 2021). At day 3 post-infection, we observed leukopenia in controls largely caused by decline in absolute counts of lymphocytes and neutrophils (Figures S2A, S2D, and S2F) with a significant decrease in relative neutrophil frequencies at day 7 in controls ($p = 0.02$), but not in treated animals ($p = 0.2$) (Figure 2A). These observations signify neutrophil infiltration into tissues consistent with inflammation in the lung.

Upon assessment of T cells, we found that the frequency of markers indicating proliferation and activation of T follicular helper (T_{fh}) cells ($Ki\text{-}67^+$, $PD\text{-}1^+$) was significantly increased in controls (Figure 2B). No other CD4 subsets, including $CXCR3^+$, Th1 CD4 T cells, or CD8 T cells, were differentially induced 7 days following infection, which could be because of delayed T cell responses in aged monkeys. We analyzed the functional capacity of T cells and observed that both CD4 and CD8 T cells responded to CD3/CD28 activation by proliferating and upregulating a panel of activation markers (Figure S3), indicating that despite the transient leukopenia, infection did not result in functional impairment of T cells, a feature observed in some infected patients (Remy et al., 2020).

We studied tissue-specific indices of T cell activation focusing on the spleen and liver as non-target lymphoid and non-lymphoid organs, respectively, at day 7 post-infection. $CD69^+$ CD4 and CD8 T cells were interrogated for activation markers, Ki-67, PD-1, HLA-DR, and granzyme B (Figure 2C). Significantly higher frequencies of CD8 T cells expressing Ki-67, PD-1, and granzyme B, but not HLA-DR (data not shown), were observed in the spleen of controls relative to mAb-treated animals. Frequencies of activated CD4 T cells were not different, and differences in T cell immune activation in the liver between the groups did not reach statistical significance. We additionally assessed dynamics of mucosal-associated invariant T cells (MAITs). Two animals in each group expressed discrete MAIT populations. We did not, however, observe differences across the groups in the liver and spleen, or observe an increase in frequency of MAITs following SARS-CoV-2 infection (Figure S4).

We also explored whether systemic biomarkers of inflammation were differentially induced between treatment groups. Plasma from controls was enriched for the anti-viral interferon (IFN)-stimulated chemokines, CXCL9, CXCL10, and CXCL11

(D) Heatmap displaying log2 normalized protein expression (NPX) values from plasma inflammatory proteins (top) and kinetics of NPX for plasma CXCL9, CXCL10, and CXCL11 (bottom). n = 4 for each experimental group/sample time point.
(E) Serum levels of anti-nuclear antibodies (ANAs) and anti-phospholipid antibodies (aPLs) in aged and young animals on days 0 and 7 pi (young, n = 4; aged, n = 8).
(F and G) Comparison of sgRNA and vRNA in (F) NSs and (G) BAL in aged and young animals on days 3 and 7 pi (young, n = 4; aged, n = 4).
Data points represent individual animals, with bars indicating medians. Gray bars indicate limit of detection. Flow data and NPX data represent a single technical replicate. *$p < 0.05$ by two-tailed (A and B) or one-tailed Mann-Whitney U test (C–G).

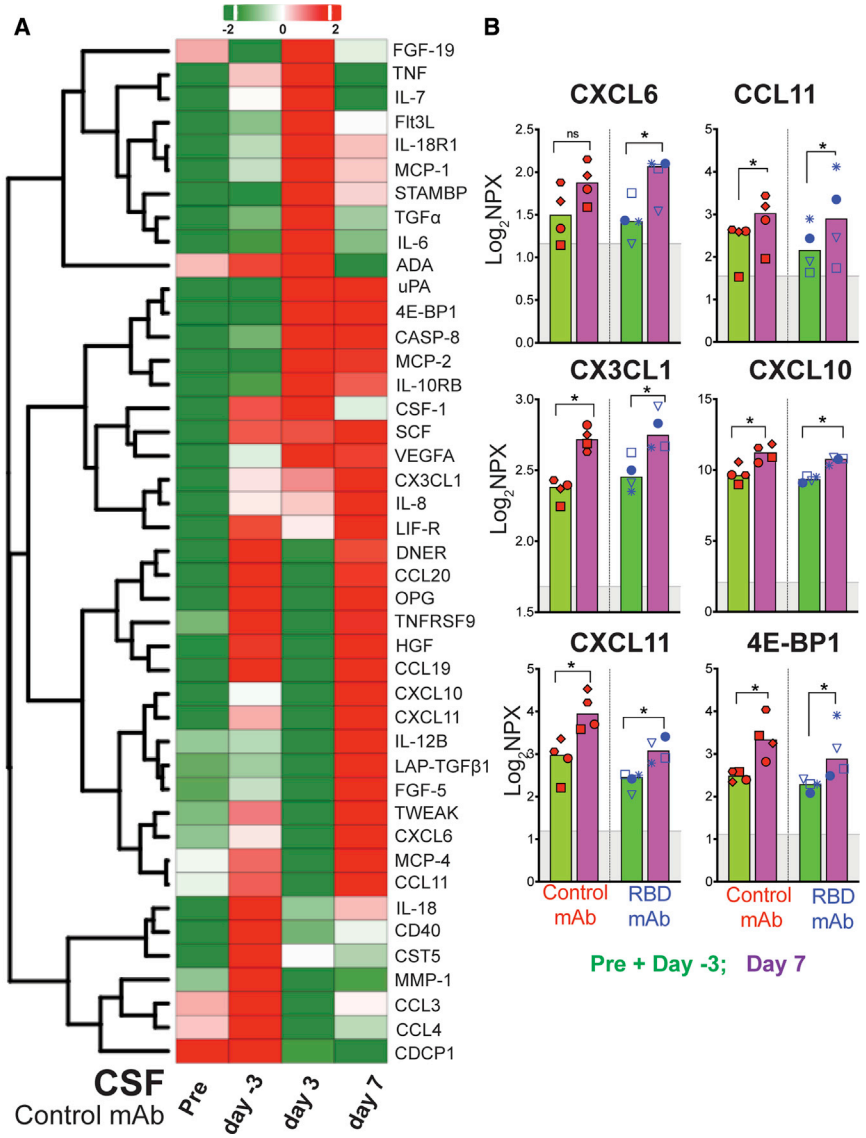

Figure 3. Immune activation in the CNS following mAb infusion

(A) Heatmap displaying log2 median values of NPX of inflammatory proteins in the CSF of control mAb-treated animals on indicated days (n = 4 for each time point). Color intensity represents standard deviation from zero mean; all values were within −2 and +2 standard deviations from zero mean.

(B) Comparison of pre-study/day −3 (median of pre-study and day −3) and day 7 NPX values of CXCL6, CXCL11, CX3CL1, MCP-4, CXCL10, CXCL11, CXCL19, and 4E-BP1 in the CSF of control and RBD mAb-treated animals. Data points represent individual animals, with bars indicating medians. NPX data represent a single technical replicate. Gray bars indicate limit of detection. *p < 0.05 by one-tailed Mann-Whitney U test.

(Figure 2D), reported to be elevated in the lungs of patients with severe COVID (Nienhold et al., 2020) and induced systemically following SARS-CoV-2 infection in animal models (Shaan Lakshmanappa et al., 2021). CXCL9 and CXCL11 levels were higher in both groups at day 7, while CXCL10 induction was specific to control animals at day 3 with significant differences across groups at days 3 and 7.

After detecting evidence of T cell activation and biomarkers of systemic inflammation, we explored whether broader indices of immune activation, such as anti-nuclear antibodies (ANAs) or anti-phospholipid antibodies (aPLs), were increased. We then asked how these observations compared in aged rhesus relative with the data we previously collected in young animals (4–5 years) post-infection (Shaan Lakshmanappa et al., 2021). We observed a modest but statistically significant induction of ANA in the aged cohort (Figure 2E). aPLs, such as those targeting cardiolipin and phosphatidylserine, have been found in the sera of 50% of hospitalized COVID-19 patients (Zuo et al., 2020). Although we did not observe evidence for thrombotic events in aged monkeys following challenge, the data revealed that aPLs were detectable at values well above the manufacturer's cutoff of 1 ng/mL prior to infection, with a significant increase in all aged macaques regardless of intervention. Notably, the levels of aPL were higher in aged macaques relative to young, infected monkeys with no co-morbidities. We did not, however, detect significant differences in vRNA in the upper and lower respiratory tracts (Figures 2F and 2G) in aged animals relative to young SARS-CoV-2-infected animals (3.4–6 years) infused with control mAb from a previous study (Van Rompay et al., 2021). Further in-depth head-to-head comparisons of histopathological lung lesions, inflammatory cytokines, and bystander T cell activation are needed to comprehensively elucidate the contribution of age to immunopathology.

Nonetheless, this pattern of inflammatory protein expression in both groups is suggestive of viral nucleic acid/protein-mediated immune activation. In light of recent studies demonstrating that the spike and envelope protein of SARS-CoV-2 stimulate TLR-2-mediated inflammatory cytokine production (Zheng et al., 2021; Khan et al., 2021), the data infer that activation of pattern recognition receptors following initial viral dosing initiated an innate inflammatory cascade despite abortive viral replication.

mAbs limit effector CD4 T cell influx in CSF

Because the constellation of inflammatory COVID-19 symptoms also involves the central nervous system (CNS), we next sought to delineate the extent of neuroinflammation following

SARS-CoV-2 infection in macaques. Based on reports of altered immune milieu in the CSF in neuro-COVID patients (Heming et al., 2021), together with cellular perturbations within the choroid plexus following SARS-CoV-2 infection (Yang et al., 2021), we focused our analysis on the CSF compartment.

Following collection of approximately 1,500–2,000 μL of CSF from the foramen magnum, samples were assessed for visible blood contamination and centrifuged to fractionate cells from the fluid. Fresh CSF cells were phenotyped, and the supernatant was frozen for subsequent assays. Measurement of RNA extracted from 0.25 mL of CSF showed no detectable SARS-CoV-2 vRNA in any CSF sample at days 3 and 7 following infection (LOD 20 copies/assay). Based on systemic inflammatory dynamics, we sought to determine the extent of the host immune response to SARS-CoV-2 within the CSF.

Proteomics analysis of CSF revealed that 43 of 92 inflammatory proteins were expressed above the LOD (Figure 3A), with six proteins exhibiting a significant induction at day 7 postchallenge. Of these chemokines responsible for recruiting neutrophils and eosinophils, chemokine ligand 6 (CXCL6) was induced in the RBD mAb group, while CXCL11 was induced in both groups at day 7 (Figure 3B). This was also observed for the monocyte and T cell chemoattractant CX3CL1. Levels of the chemokines CXCL10 and CXCL11 stimulated by the presence of IFN were increased in both groups. Notably, the levels of CXCL11 and MCP-4 in the CSF correlated with their respective plasma levels. Induction of the eukaryotic initiation factor 4E-binding protein (4E-BP1), which controls lymphocyte cell proliferation (So et al., 2016), led us to question whether the concentration of effector T cells increased within the CSF following challenge. Indeed, CSF is permissive to T cell effectors, and studies in patients with neuro-COVID document a monocyte and T cell signature within the CSF (Heming et al., 2021).

Using samples not visibly contaminated with blood (>98% of samples), we obtained, on average, 20,000 cells/CSF sample prior to infection (range: 13,000–30,000) and 20,000 cells at day 7 (range: 7,000–43,000) (Figure S5). Consistent with observations in COVID-19 patients (Destras et al., 2020), CSF samples were uniformly negative for vRNA at days 3 and 7 post-infection. As observed with the phenotype of cells in human CSF, the majority of CD4 and CD8 T cells were $CD28^{+}CD95^{+}$, consistent with the central memory phenotype (Figure 4A). Evaluation of Ki-67^{+} T cells showed that frequencies at baseline ranged from 2% to 10%. Following infection, we observed a 3-fold increase in Ki-67^{+} CD4 T cells at day 7 in controls with significant differences between the controls and the mAb group (Figure 4B). Assessment of the phenotype of Ki-67^{+} CD4 T cells in controls revealed moderate expression of the activation markers CD25, CD69, and TIGIT, while most cells were PD-1^{+}, suggesting T cell receptor-dependent activation (Figure 4C). Activated CD4 T cell frequencies in CSF were highly correlated with activated CD4 T cell frequencies within the mediastinal lymph node (Figure 4D).

Whether this increased influx of effector T cells is responsible for the neuroinflammatory and CNS sequalae observed in a subset of COVID-19 patients is a question that merits investigation. Production of pro-inflammatory cytokines such as IFNγ and proteases by effector CD4 T cells degrades the glia limitans, facilitating immune cell influx into the brain parenchyma, rendering neurons susceptible to inflammation-induced injury (Engelhardt and Coisne, 2011). Furthermore, IFNγ can activate brain and choroid plexus macrophages potentiating the neuroinflammatory response and, when unchecked, can result in neuronal injury ultimately contributing to neurological disease (Papageorgiou et al., 2016). Measurement of neurofilament protein concentrations, a biomarker of axonal injury, and other soluble biomarkers of immune activation in the CSF, such as neopterin in larger and long-term animal studies of COVID-19, may reveal additional insights into the nexus between CSF inflammatory profiles and neuronal injury.

Limitations of the study

Altogether, our data support the conclusion that RBD mAbs block SARS-CoV-2 replication, development of interstitial pneumonia, and effector CD4 T cell influx into CSF in aged diabetic rhesus macaques. However, our study has several limitations. First, treatment efficacy within the context of other comorbidities, such as chronic lung diseases, cardiovascular diseases, and immune suppression, which increase vulnerability to severe COVID-19, were not assessed (Thakkar et al., 2021). In addition to comorbidities, COVID-19 also exhibits sex biases, with male patients being more susceptible to developing severe disease; hence future studies evaluating RBD-mAb therapy in male animals would be informative. Second, other factors, such as innate responses and host anti-viral responses, may be more challenging to discern because of variation in early viral replication and viral clearance (Neidleman et al., 2021). Thus, incorporating larger sample sizes may provide deeper insights into the effects of RBD-mAb on early immune dynamics. Lastly, our study utilizes the WA1 isolate of SARS-CoV-2. The increasing number of variants of concern has led to the identification of viral strains with increased replication rates and enhanced infectivity that can increase antigen load and subsequent immune activation driving enhanced pathogenesis. Thus, it is important to determine whether WA1-specific RBD-mAbs are effective against these concerning variants.

In summary, the data demonstrate that mAbs block the establishment of SARS-CoV-2 infection in the upper and lower respiratory tracts, reduce effector T cell differentiation within lymph nodes, resulting in reduced effector T cells in blood and CSF, and markedly reduce development of histopathological lesions in the lung. Our data corroborate predictive associations between neutralizing antibody levels and protection in clinical cohorts (Khoury et al., 2021) and experimentally reinforce the concept that neutralizing mAbs confer protection against infection and disease. Of relevance to populations at high risk for severe COVID, our data show that neutralizing antibodies can mitigate the adverse inflammatory sequalae of viral infection within the lung, systemically, and within the CNS in the elderly, thus reducing adverse clinical outcomes.

STAR★METHODS

Detailed methods are provided in the online version of this paper and include the following:

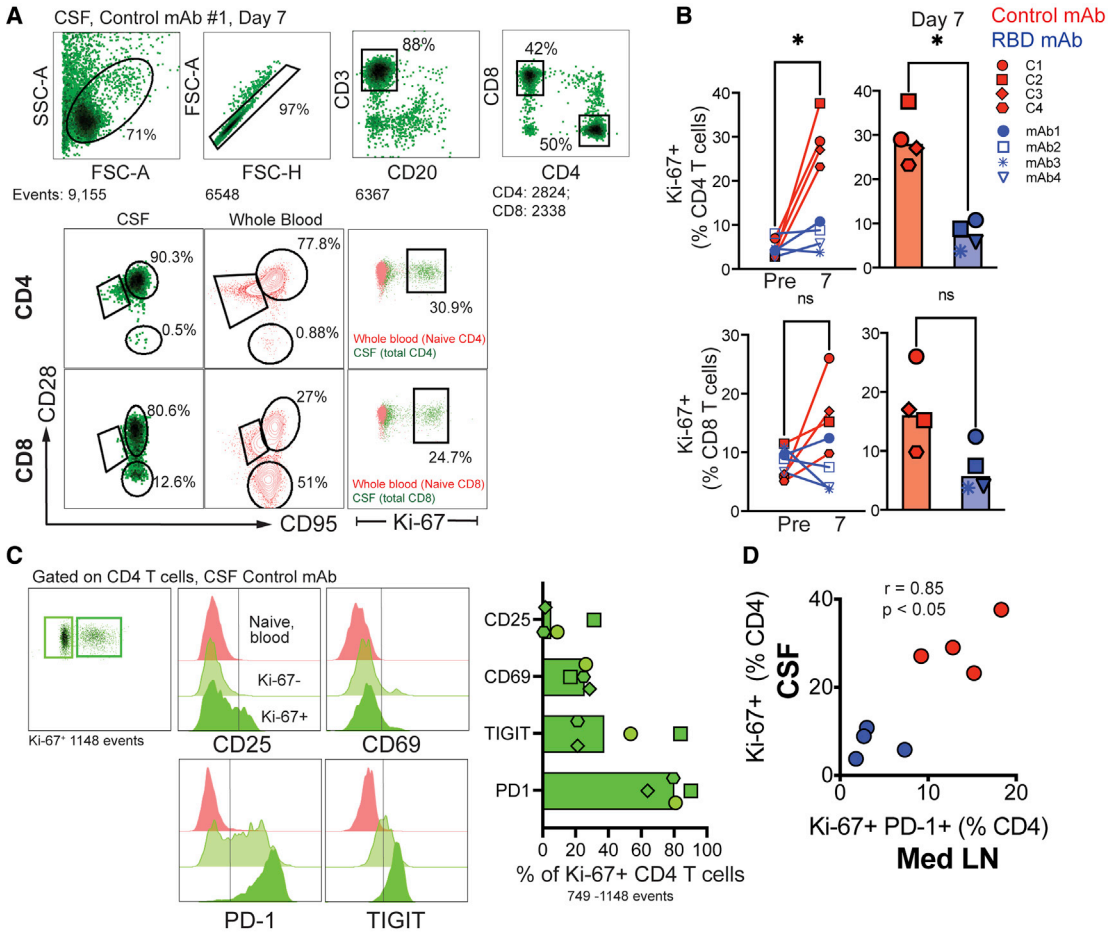

Figure 4. mAbs limit effector CD4 T cell influx in the CSF

(A) Gating strategy and flow cytometry analysis of Ki-67 expression in CD28^{+}CD95^{+} (central memory), CD28^{-}CD95^{+} (effector memory), and CD28^{+}CD95^{-} (naive) CD4 and CD8 T cell subsets in the CSF (green) and whole blood (red).

(B) Frequency of Ki-67^{+} CD4 and CD8 T cells in the CSF.

(C) Median fluorescent intensity (MFI) and frequency of Ki-67^{+}/Ki-67^{-} CD4 T cell subsets expressing activation markers (CD25, CD69, PD-1, and TIGIT) in the CSF.

(D) Spearman correlation shows frequencies of activated CD4 T cells in CSF correlate with activated CD4 T cells in mediastinal lymph node at day 7 ($r = 0.85$; $p < 0.05$; $n = 8$).

Data points represent individual animals, with bars indicating medians. Flow data represent a single technical replicate. *$p < 0.05$ by two-tailed Mann-Whitney U test (B).

SUPPLEMENTAL INFORMATION

Supplemental information can be found online at https://doi.org/10.1016/j.celrep.2021.109942.

ACKNOWLEDGMENTS

This study was supported by NIH grant R21 AI143454-02S1 (to S.S.I.), FAST GRANT–George Mason University (to S.S.I.), NIH grant 3RF1AG061001-01S1 (to S.S.I. and J.H.M.), and the CNPRC base grant P51OD011107. The figures were created with BioRender.com.

AUTHOR CONTRIBUTIONS

S.S.I., J.H.M., and K.K.A.V.R. designed the study. S.S.I., K.K.A.V.R., D.H.-O., and L.L.C. supervised experiments. P.A.K., B.A.S., J.W.R., A.V., Y.S.L., and S.S.I. performed experiments. Z.-M.M., J.R.R., and K.J.O. performed histopathology. R.L.S. and R.P. provided veterinary care and clinical assessments. M.N. provided critical reagents. B.A.S., C.E.H., and S.S.I. analyzed data. S.S.I., A.V., and C.E.H. wrote the manuscript. All authors edited the manuscript.

DECLARATION OF INTERESTS

The authors declare no competing interests.

Received: July 3, 2021
Revised: August 20, 2021
Accepted: October 13, 2021
Published: October 19, 2021

REFERENCES

Assarsson, E., Lundberg, M., Holmquist, G., Björkesten, J., Thorsen, S.B., Ekman, D., Eriksson, A., Rennel Dickens, E., Ohlsson, S., Edfeldt, G., et al. (2014). Homogenous 96-plex PEA immunoassay exhibiting high sensitivity, specificity, and excellent scalability. PLoS ONE *9*, e95192.

Baum, A., Ajithdoss, D., Copin, R., Zhou, A., Lanza, K., Negron, N., Ni, M., Wei, Y., Mohammadi, K., Musser, B., et al. (2020). REGN-COV2 antibodies prevent and treat SARS-CoV-2 infection in rhesus macaques and hamsters. Science *370*, 1110–1115.

Chandrashekar, A., Liu, J., Martinot, A.J., McMahan, K., Mercado, N.B., Peter, L., Tostanoski, L.H., Yu, J., Maliga, Z., Nekorchuk, M., et al. (2020). SARS-CoV-2 infection protects against rechallenge in rhesus macaques. Science *369*, 812–817.

Chang, M.C., Hild, S., and Grieder, F. (2021). Nonhuman primate models for SARS-CoV-2 research: Consider alternatives to macaques. Lab Anim. (NY) *50*, 113–114.

Channappanavar, R., and Perlman, S. (2020). Age-related susceptibility to coronavirus infections: role of impaired and dysregulated host immunity. J. Clin. Invest. *130*, 6204–6213.

Cohen, M.S., Nirula, A., Mulligan, M.J., Novak, R.M., Marovich, M., Yen, C., Stemer, A., Mayer, S.M., Wohl, D., Brengle, B., et al. (2021). Effect of Bamlanivimab vs Placebo on Incidence of COVID-19 Among Residents and Staff of Skilled Nursing and Assisted Living Facilities: A Randomized Clinical Trial. JAMA *326*, 46–55.

Dagotto, G., Mercado, N.B., Martinez, D.R., Hou, Y.J., Nkolola, J.P., Carnahan, R.H., Crowe, J.E., Jr., Baric, R.S., and Barouch, D.H. (2021). Comparison of Subgenomic and Total RNA in SARS-CoV-2 Challenged Rhesus Macaques. J. Virol. *95*, e02370-20.

Destras, G., Bal, A., Escuret, V., Morfin, F., Lina, B., and Josset, L.; COVID-Diagnosis HCL Study Group (2020). Systematic SARS-CoV-2 screening in cerebrospinal fluid during the COVID-19 pandemic. Lancet Microbe *1*, e149.

Dror, A.A., Eisenbach, N., Taiber, S., Morozov, N.G., Mizrachi, M., Zigron, A., Srouji, S., and Sela, E. (2020). Vaccine hesitancy: the next challenge in the fight against COVID-19. Eur. J. Epidemiol. *35*, 775–779.

Engelhardt, B., and Coisne, C. (2011). Fluids and barriers of the CNS establish immune privilege by confining immune surveillance to a two-walled castle moat surrounding the CNS castle. Fluids Barriers CNS *8*, 4.

Haas, E.J., Angulo, F.J., McLaughlin, J.M., Anis, E., Singer, S.R., Khan, F., Brooks, N., Smaja, M., Mircus, G., Pan, K., et al. (2021). Impact and effectiveness of mRNA BNT162b2 vaccine against SARS-CoV-2 infections and COVID-19 cases, hospitalisations, and deaths following a nationwide vaccination campaign in Israel: an observational study using national surveillance data. Lancet *397*, 1819–1829.

Hall, V.J., Foulkes, S., Saei, A., Andrews, N., Oguti, B., Charlett, A., Wellington, E., Stowe, J., Gillson, N., Atti, A., et al.; SIREN Study Group (2021). COVID-19 vaccine coverage in health-care workers in England and effectiveness of BNT162b2 mRNA vaccine against infection (SIREN): a prospective, multicentre, cohort study. Lancet *397*, 1725–1735.

Heming, M., Li, X., Räuber, S., Mausberg, A.K., Börsch, A.L., Hartlehnert, M., Singhal, A., Lu, I.N., Fleischer, M., Szepanowski, F., et al. (2021). Neurological Manifestations of COVID-19 Feature T Cell Exhaustion and Dedifferentiated Monocytes in Cerebrospinal Fluid. Immunity *54*, 164–175.e6.

Khan, S., Shafiei, M.S., Longoria, C., Schoggins, J., Savani, R.C., and Zaki, H. (2021). SARS-CoV-2 spike protein induces inflammation via TLR2-dependent activation of the NF-kappaB pathway. bioRxiv. https://doi.org/10.1101/2021.03.16.435700.

Khoury, D.S., Cromer, D., Reynaldi, A., Schlub, T.E., Wheatley, A.K., Juno, J.A., Subbarao, K., Kent, S.J., Triccas, J.A., and Davenport, M.P. (2021). Neutralizing antibody levels are highly predictive of immune protection from symptomatic SARS-CoV-2 infection. Nat. Med. *27*, 1205–1211.

Kim, C., Ryu, D.K., Lee, J., Kim, Y.I., Seo, J.M., Kim, Y.G., Jeong, J.H., Kim, M., Kim, J.I., Kim, P., et al. (2021). A therapeutic neutralizing antibody targeting receptor binding domain of SARS-CoV-2 spike protein. Nat. Commun. *12*, 288.

Lakshmanappa, Y.S., Roh, J.W., Rane, N.N., Dinasarapu, A.R., Tran, D.D., Velu, V., Sheth, A.N., Ofotokun, I., Amara, R.R., Kelley, C.F., et al. (2021). Circulating integrin $\alpha_4\ \beta_7\ ^+$ CD4 T cells are enriched for proliferative transcriptional programs in HIV infection. FEBS Lett. *595*, 2257–2270.

Mathieu, E., Ritchie, H., Ortiz-Ospina, E., Roser, M., Hasell, J., Appel, C., Giattino, C., and Rodés-Guirao, L. (2021). A global database of COVID-19 vaccinations. Nat. Hum. Behav. *5*, 947–953.

Moghadas, S.M., Vilches, T.N., Zhang, K., Wells, C.R., Shoukat, A., Singer, B.H., Meyers, L.A., Neuzil, K.M., Langley, J.M., Fitzpatrick, M.C., et al. (2020). The impact of vaccination on COVID-19 outbreaks in the United States. medRxiv. https://doi.org/10.1101/2020.11.27.20240051.

Neidleman, J., Luo, X., George, A.F., McGregor, M., Yang, J., Yun, C., Murray, V., Gill, G., Greene, W.C., Vasquez, J., et al. (2021). Distinctive features of SARS-CoV-2-specific T cells predict recovery from severe COVID-19. Cell Reports *36*. https://doi.org/10.1016/j.celrep.2021.109414.

Nienhold, R., Ciani, Y., Koelzer, V.H., Tzankov, A., Haslbauer, J.D., Menter, T., Schwab, N., Henkel, M., Frank, A., Zsikla, V., et al. (2020). Two distinct immunopathological profiles in autopsy lungs of COVID-19. Nat. Commun. *11*, 5086.

Papageorgiou, I.E., Lewen, A., Galow, L.V., Cesetti, T., Scheffel, J., Regen, T., Hanisch, U.K., and Kann, O. (2016). TLR4-activated microglia require IFN-γ to induce severe neuronal dysfunction and death in situ. Proc. Natl. Acad. Sci. USA *113*, 212–217.

Raja, A.S., Niforatos, J.D., Anaya, N., Graterol, J., and Rodriguez, R.M. (2021). Vaccine hesitancy and reasons for refusing the COVID-19 vaccination among the U.S. public: A cross-sectional survey. medRxiv. https://doi.org/10.1101/2021.02.28.21252610.

Remy, K.E., Mazer, M., Striker, D.A., Ellebedy, A.H., Walton, A.H., Unsinger, J., Blood, T.M., Mudd, P.A., Yi, D.J., Mannion, D.A., et al. (2020). Severe immunosuppression and not a cytokine storm characterizes COVID-19 infections. JCI Insight *5*, e140329.

Robbiani, D.F., Gaebler, C., Muecksch, F., Lorenzi, J.C.C., Wang, Z., Cho, A., Agudelo, M., Barnes, C.O., Gazumyan, A., Finkin, S., et al. (2020). Convergent antibody responses to SARS-CoV-2 in convalescent individuals. Nature *584*, 437–442.

Shaan Lakshmanappa, Y., Elizaldi, S.R., Roh, J.W., Schmidt, B.A., Carroll, T.D., Weaver, K.D., Smith, J.C., Verma, A., Deere, J.D., Dutra, J., et al.

(2021). SARS-CoV-2 induces robust germinal center CD4 T follicular helper cell responses in rhesus macaques. Nat. Commun. *12*, 541.

Shi, R., Shan, C., Duan, X., Chen, Z., Liu, P., Song, J., Song, T., Bi, X., Han, C., Wu, L., et al. (2020). A human neutralizing antibody targets the receptor-binding site of SARS-CoV-2. Nature *584*, 120–124.

Singh, D.K., Singh, B., Ganatra, S.R., Gazi, M., Cole, J., Thippeshappa, R., Alfson, K.J., Clemmons, E., Gonzalez, O., Escobedo, R., et al. (2021). Responses to acute infection with SARS-CoV-2 in the lungs of rhesus macaques, baboons and marmosets. Nat. Microbiol. *6*, 73–86.

So, L., Lee, J., Palafox, M., Mallya, S., Woxland, C.G., Arguello, M., Truitt, M.L., Sonenberg, N., Ruggero, D., and Fruman, D.A. (2016). The 4E-BP-eIF4E axis promotes rapamycin-sensitive growth and proliferation in lymphocytes. Sci. Signal. *9*, ra57.

Thakkar, A., Gonzalez-Lugo, J.D., Goradia, N., Gali, R., Shapiro, L.C., Pradhan, K., Rahman, S., Kim, S.Y., Ko, B., Sica, R.A., et al. (2021). Seroconversion rates following COVID-19 vaccination among patients with cancer. Cancer Cell *39*, 1081–1090.e2.

Van Rompay, K.K.A., Olstad, K.J., Sammak, R.L., Dutra, J., Watanabe, J.K., Usachenko, J.L., Immareddy, R., Verma, A., Shaan Lakshmanappa, Y., Schmidt, B.A., et al. (2021). Early treatment with a combination of two potent neutralizing antibodies improves clinical outcomes and reduces virus replication and lung inflammation in SARS-CoV-2 infected macaques. PLoS Pathog. *17*, e1009688.

Yang, Y., Shen, C., Li, J., Yuan, J., Wei, J., Huang, F., Wang, F., Li, G., Li, Y., Xing, L., et al. (2020). Plasma IP-10 and MCP-3 levels are highly associated with disease severity and predict the progression of COVID-19. J. Allergy Clin. Immunol. *146*, 119–127.e4.

Yang, A.C., Kern, F., Losada, P.M., Agam, M.R., Maat, C.A., Schmartz, G.P., Fehlmann, T., Stein, J.A., Schaum, N., Lee, D.P., et al. (2021). Dysregulation of brain and choroid plexus cell types in severe COVID-19. Nature *595*, 565–571.

Zheng, M., Karki, R., Williams, E.P., Yang, D., Fitzpatrick, E., Vogel, P., Jonsson, C.B., and Kanneganti, T.D. (2021). TLR2 senses the SARS-CoV-2 envelope protein to produce inflammatory cytokines. Nat. Immunol. *22*, 829–838.

Zost, S.J., Gilchuk, P., Case, J.B., Binshtein, E., Chen, R.E., Nkolola, J.P., Schäfer, A., Reidy, J.X., Trivette, A., Nargi, R.S., et al. (2020). Potently neutralizing and protective human antibodies against SARS-CoV-2. Nature *584*, 443–449.

Zuo, Y., Estes, S.K., Ali, R.A., Gandhi, A.A., Yalavarthi, S., Shi, H., Sule, G., Gockman, K., Madison, J.A., Zuo, M., et al. (2020). Prothrombotic autoantibodies in serum from patients hospitalized with COVID-19. Sci. Transl. Med. *12*, eabd3876.

STAR★METHODS

KEY RESOURCES TABLE

REAGENT or RESOURCE	SOURCE	IDENTIFIER
Antibodies		
Mouse anti-human CD3 (Clone SP34-2)	BD Biosciences	Cat#557917; RRID: AB_396938
Mouse anti-human CD3 (Clone SP34-2)	BD Biosciences	Cat#557757; RRID: AB_396863
Mouse anti-human CD4 (Clone L200)	BD Biosciences	Cat#563737; RRID: AB_2687486
Mouse anti-human CD8 (Clone SK-1)	BD Biosciences	Cat#564913; RRID: AB_2833078
Mouse anti-human CD11c (Clone 3.9)	Invitrogen	Cat#25-0116-42; RRID: AB_1582274
Mouse anti-human CD14 (Clone MSE2)	BioLegend	Cat#301822; RRID: AB_493747
Mouse anti-human CD16 (Clone 3G8)	BD Biosciences	Cat#563172; RRID: AB_2744297
Mouse anti-human CD20 (Clone 2H7)	BioLegend	Cat#302328; RRID: AB_1595435
Mouse anti-human CD20 (Clone 2H7)	BioLegend	Cat#302314; RRID: AB_314262
Mouse anti-human CD25 (Clone BC96)	Tonbo Biosciences	Cat#20-0259; RRID: AB_2621758
Mouse anti-human CD28 (Clone CD28.2)	BioLegend	Cat#302942; RRID: AB_256435
Mouse anti-human CD66 (Clone TET2)	Miltenyi Biotec	Cat#130-118-539; RRID: AB_2733398
Mouse anti-human CD69 (Clone FN50)	BioLegend	Cat#310944; RRID: AB_2566466
Mouse anti-human CD95 (Clone DX2)	BD Biosciences	Cat#564710; RRID: AB_2738907
Mouse anti-human CD154 (SLAM) (Clone A12-7D4)	BioLegend	Cat#306312; RRID: AB_2187945
Mouse anti-human CXCR3 (CD183) (Clone 1C6)	BD Biosciences	Cat#741005; RRID: AB_2740628
Mouse anti-human CXCR5 (CD185) (Clone MU5UBEE)	Thermofisher	Cat#12-9185-42; RRID: AB_11219877
Rat anti-human CX3CR1 (Clone 2A9-1)	BioLegend	Cat#341624; RRID: AB_2687152
Mouse anti-human CCR6 (CD196) (Clone G034E3)	BioLegend	Cat#353430; RRID: AB_2564233
Mouse anti-human PD1 (CD279) (Clone EH12.2H8)	BioLegend	Cat#329918; RRID: AB_2159324
Mouse anti-Ki-67 (Clone B56)	BD Biosciences	Cat#558616; RRID: AB_10611866
Armenian Hamster anti- ICOS (CD278) (Clone C396.4A)	BioLegend	Cat#313534; RRID: AB_2629729
Recombinant anti-$\alpha 4\beta 7$ (Clone A4B7R1)	NHP Reag Res	Cat#PR-1422; RRID: AB_2819258
Mouse anti-human TIGIT (Clone MBSA43)	ThermoFisher	Cat#12-9500-42; RRID: AB_10714831
Mouse anti-GranzymeB (Clone GB11)	BioLegend	Cat#515408; RRID: AB_2562196
Mouse anti-Foxp3 (Clone 206D)	BioLegend	Cat#320114; RRID: AB_439754
Mouse anti-human HLA-DR (Clone L243)	BioLegend	Cat#307642; RRID: AB_2563461
APC-Cy7 live/dead	Life Technologies	Cat#L34976; RRID: N/A
BV510 live/dead	Life Technologies	Cat#L34966 Cat#L34966; RRID: N/A
Rabbit anti-SARS- NP	Novus Biologicals	Cat#NB100-56576; RRID: AB_838838
Rat anti-CD3 (Clone CD3-12)	Abcam	Cat#ab11089; RRID: AB_2889189
Mouse anti-CD68 (Clone KP1)	Thermofisher	Cat#MS-397-P0; RRID: AB_720547
Bacterial and virus strains		
SARS-CoV-2 2019-nCoV/USA-WA1/2020	BEI Resources	NR-52352
Biological samples		
Rhesus macaque biological fluids (blood, nasal aspirate, BALF, and CSF)	CNPRC, University of California Davis	N/A

(*Continued on next page*)

Continued

REAGENT or RESOURCE	SOURCE	IDENTIFIER
Rhesus macaque primary cells (spleen, liver, PBMCs, and lymph node cells)	CNPRC, University of California Davis	N/A
Rhesus macaque lung lobes tissue	CNPRC, University of California Davis	N/A
Chemicals, peptides, and recombinant proteins		
Luciferase Cell Culture Lysis reagent	Promega	Cat#E1531
DAPI (4',6-diamidino-2-phenylindole, dihydrochloride)	Thermofisher	Cat#62247
FoxP3/ Transcription Factor Staining Buffer set	Invitrogen	Cat#00-5523
Brilliant stain buffer	BD Biosciences	Cat#563794
Cytofix/cytoperm	BD Biosciences	Cat#51-2090K2
51427 Mamu MR1 5-OP-RU - PE	NIH Tetramer Core Facility, Emory University	N/A
51428 Mamu MR1 6-FP - PE	NIH Tetramer Core Facility, Emory University	N/A
SARS CoV-2 S1 protein	Sino Biologicals	Cat#40591-V08H
SARS CoV-2 S2 extracellular domain protein	Sino Biologicals	Cat#40590-V08B
SARS CoV-2 nucleocapsid (N) protein	Sino Biologicals	Cat#40588-V08B
Critical commercial assays		
Cell Trace Violet (CTV) assay kit	Invitrogen	Ref#C34557
T cell activation/expansion kit (NHP)	Miltenyi Biotec	Cat#130-092-919
Monkey Anti-Nuclear Antibody ELISA kit	MyBioSource	Cat#MBS749189
Monkey Anti phospholipid Antibody ELISA kit	MyBioSource	Cat#MBS738451
Monkey ACE2 ELISA Kit	MyBioSource	Cat#MBS2514879
Experimental models: Organisms/strains		
Rhesus macaque (Macaca mulatta)	CNPRC, University of California Davis	N/A
Oligonucleotides		
orf1a_F7 (GTGCTCATGGATGGCTCTATTA)	Van Rompay et al., 2021	N/A
orf1a_R7 (CGTGCCTACAGTACTCAGAATC)	Van Rompay et al., 2021	N/A
orf1a_P7 (/56FAM/ACCTACCTT/ZEN/ GAAGGTTCTGTTAGAGTGGT/3IABkFQ/)	Van Rompay et al., 2021	N/A
sgLeadSARSCoV2_F (CGATCTCTTGTAGATCTGTTCTC)	Van Rompay et al., 2021	N/A
wtN_R4 (GGTGAACCAAGACGCAGTAT)	Van Rompay et al., 2021	N/A
wtN_P4 (/56-FAM/TAACCAGAA/ZEN/ TGGAGAACGCAGTGGG/3IABkFQ/)	Van Rompay et al., 2021	N/A
wtN_F4 (GTTTGGTGGACCCTCAGATT)	Van Rompay et al., 2021	N/A
Software and algorithms		
GraphPad Prism (version 8.4.2)	GraphPad	https://www.graphpad.com/
FACS Diva (version 8.0.1)	BD Biosciences	https://www.bdbiosciences.com/en-u
FlowJo (version 10 or 10.6.3)	FlowJo LLC	https://www.flowjo.com
R (version 3.3.3)	R Core Team	https://www.r-project.org
Other		
Cell Preparation Tubes (CPT)	BD	Cat#362761

RESOURCE AVAILABILITY

Lead contact

Further information and request for resources and reagents should be directed to and will be fulfilled by the Lead Contact, Dr. Smita S. Iyer (smiyer@ucdavis.edu).

Materials availability

This study did not generate new unique reagents.

Data and code availability

The published article includes all data generated during this study. This paper does not report original code.

Any additional information required to reanalyze the data reported in this paper is available from the lead contact upon request.

EXPERIMENTAL MODEL AND SUBJECT DETAILS

Rhesus Macaques

Eight colony-bred Indian-origin rhesus macaques (Macaca mulatta) were housed at the California National Primate Research Center and maintained in accordance with American Association for Accreditation of Laboratory Animal Care guidelines and Animal Welfare Act/Guide. All study procedures were approved by the Institutional Animal Care and Use Committee at UC Davis. Animals (n = 8) were geriatric female rhesus macaques with a clinical diagnosis of diabetes (Table S1). They were between 18 and 23 years of age and all required insulin to regulate their blood glucose. They were divided into 2 groups with similar average age, body condition score, and glycosylated hemoglobin values. In addition to diabetes, multiple animals were clinically suspected to have GI adenocarcinoma, 3 animals were hypertensive (systolic > 140 mmHg), and 1 animal was being treated for endometriosis with deslorelin. Animals continued their insulin therapy along with any oral glucose control medications during the study period. All 8 animals were randomized into sampling groups (n = 2, one each from RBD mAb and control groups) to minimize sampling bias.

Clinical Assessments

Clinical assessments were performed by a board-certified laboratory animal veterinarian at baseline and on each day of the project. Animals were observed for any abnormalities and changes in activity, respiration, appetite, stool. At each sedated time point, 4 view radiographs were obtained (MinXray, Northbrook, IL), blood pressure was measured via oscillometry (Sun Tech, Morrisville, NC), temperature was taken, and pulse oximetry was measured (Masimo, Irvine, CA). Radiographs were interpreted by a board-certified veterinary radiologist with time point and treatment condition masked.

Monoclonal antibodies and administration

SARS-CoV-2 neutralizing antibody clones C144-LS and C135-LS (half-maximal inhibitory concentrations IC_{50} of 2.55 and 2.98 ng/mL against the virus isolate Wuhan-Hu-1' (GenBank: NC_045512) isolated from convalescent COVID-19 patients (Robbiani et al., 2020) were administered in combination (1:1). Animals in the control group received mAb against the CD4 binding site of HIV gp120 envelope protein (3BNC117). mAbs were dosed at 20 mg/kg each and were administered intravenously at a rate of 2mL/ minute.

Virus and inoculations

Animals were inoculated with a total of 2.5 mL ($2.5x10^6$ PFU) SARS-CoV-2: 2 mL intratracheal and 0.5 mL intranasally (0.25 mL per nostril). The WA isolate from BEI Resources (SARS-CoV-2 2019-nCoV/USA-WA1/2020; NR-52352; Lot/Batch # 70033952) was used directly for inoculations.

Specimen collection and processing

Animals were anesthetized with 10 mg/kg ketamine hydrochloride injected intramuscularly prior to sample collection. EDTA-anticoagulated blood was collected at baseline (pre-project), days −3, 0, 3 and 7 for immunophenotyping. PBMCs were isolated from whole blood collected in CPT vacutainer tubes, sampled at day −3 and necropsy (day 7), by density gradient centrifugation. For serum, coagulated blood was centrifuged at 800 g for 10 min to pellet clotted cells, supernatant was extracted and stored at −80°C. For collection of cerebrospinal fluid (CSF), following anesthesia and palpation of the site between vertebrae, CSF was aspirated using a sterile needle up to a maximum of 0.5 mL/kg body weight or 2 mL/animal. The CSF was placed on ice until processing. After separation of cells from supernatant, cells were resuspended in 200 μL of complete media until staining for flow cytometry. CSF supernatant was frozen down. Lymph nodes, spleen, and liver tissue were obtained at necropsy and digested enzymatically using collagenase followed by manual disruption to obtain single cell suspensions for flow cytometry-based assays. The remaining cells were cryopreserved using freezing solution of 90% FBS and 10% DMSO in LN.

METHOD DETAILS

Inflammatory analytes

For measurement of inflammatory analytes, triton inactivated samples were shipped to Olink Proteomics at Stanford University. A 92-biomarker inflammation panel was run according to manufacturer's instructions. Protein levels are expressed as normalized protein expression (NPX) values, an arbitrary unit. Inflammatory analytes in BALF, CSF, plasma were analyzed using a proximity extension assay (O link, Proteomics) as described (Assarsson et al., 2014).

Serum biochemistry

Biochemistry analysis on serum samples was performed using Piccolo® BioChemistry Plus disks, that were run on the Piccolo® Xpress Chemistry Analyzer (Abbott), according to the manufacturer's instructions. This panel includes alanine aminotransferase (ALT), albumin, alkaline phosphatase (ALP), amylase, aspartate aminotransferase (AST), C-reactive protein, calcium, creatinine, gamma glutamyl transferase (GGT), glucose, total protein, blood urea nitrogen (BUN), and uric acid.

Virology

To determine viral RNA levels, quantitative real-time PCR (qRT-PCR) previously developed against full-length genomic vRNA (gRNA), sub-genomic vRNA (sgRNA), and total vRNA were used (Shaan Lakshmanappa et al., 2021). RNA was extracted from swabs preserved in DNA/RNA Shield using the Quick-RNA Viral Kit (Zymo Research) per manufacturer's recommendations. Tissues preserved in RNAlater were transferred to Qiazol and homogenized with a 7mm stainless steel bead in a TissueLyser (QIAGEN) and processed using the QIAGEN RNeasy Mini Kit using manufacturer's recommendations. Following DNase treatment with ezDNase (ThermoFisher), complementary DNA was generated using random hexamers, Superscript IV Reverse Transcriptase (ThermoFisher) in the presence of RNaseOUT (ThermoFisher). A portion of this reaction was mixed with QuantiTect Probe PCR Kit and optimized concentrations of gene specific primers. qRT-PCR reactions were performed on a Quantstudio 12K Flex real-time cycler (Applied Biosystems). gRNA was quantified by targeting orf1a-nsp4 using **primers orf1a_F7** (GTGCTCATGGATGGCTCTATTA) and orf1a_R7 (CGTGCCTACAGTACTCAGAATC), with probe orf1a_P7 (/56-FAM/ACCTACCTT/ZEN/GAAGGTTCTGTTAGAGTGGT/3IABkFQ/). sgRNA was quantified using primers sgLeadSARSCoV2_F (CGATCTCTTGTAGATCTGTTCTC) and wtN_R4 (GGTGAACCAAGACG CAGTAT), with probe wtN_P4 (/56-FAM/TAACCAGAA/ZEN/TGGAGAACGCAGTGGG/3IABkFQ/). Total vRNA was quantified using primers wtN_F4 (GTTTGGTGGACCCTCAGATT) and wtN_R4, with probe wtN_P4. Standard curves generated from PCR amplicons of the qRT-PCR targets were used to establish line equations to determine RNA copies/mL or copies/ug RNA. A macaca housekeeping gene PPIA was used as a reference (TaqMan Gene Expression Assays Rh02832197_gH, PPIA; Applied Biosystems PN4351370). The limit of detection of RTqPCR for nasal swabs was set at 20 copies/swab. For tissues, the LOD was set at 0.8 copies/mg tissue

For plaque assays, tissues frozen at −80°C were used. Briefly, the frozen tissue was weighed and 500 μL DMEM was added to each tube with a 5mm glass bead. The tissue was homogenized at 30Hz for 4 minutes. Following 2 rounds of homogenization, tissue was centrifuged at 12,000 rpm for 4 minutes. Supernatants of homogenates were assayed using Vero-81 cells in 12-well plates in serial 10-fold dilutions beginning at 1:10. Each sample was titrated in duplicate and the average value is reported. Based on the volume and dilution of sample tested, the LOD for plaque assays was 40 PFU/ml of triturated supernatant, or 0.2 PFU/mg tissue.

Flow cytometry and immunofluorescent staining

Whole blood samples were stained fresh and acquired the same day. Staining on spleen, lymph node, liver, and PBMCs was performed on cryopreserved samples. Fluorescence was measured using a BD Biosciences FACSymphony or BD Biosciences LSR Fortessa with FACS Diva version 8.0.1 software. Compensation, gating, and analysis were performed using FlowJo (Version 10). For immunofluorescence imaging, 4 μm cut sections of the caudal lung lobe on slides were stained with Rat anti-CD3 (Abcam), Mouse anti-CD68 (Thermofisher), and Rabbit anti-SARS N (Novus) along with goat anti-rat Alexa fluor 488, goat anti-rabbit Alexa fluor 568, and goat anti-mouse Alexa fluor 647. Irrelevant antibodies with Isotype IgG of rat, mouse, and rabbit were used as negative controls. Positive sections and sections of uninfected lung samples were processed with the experimental slides at the same time. Coverslips were placed on all slides using the ProLong Gold Antifade Mountant with 4′,6-diamidino-2-phenylindole (DAPI) as a nuclear stain (Molecular Probes, Grand Island, NY). The slides were viewed, and images were captured with epifluorescent illumination using a Zeiss Imager Z1 microscope (Carl Zeiss Inc., Thornwood, NY) with appropriate filter.

Serology

A customized binding antibody multiplex assay (BAMA) was used to measure IgM serum antibodies to the following recombinant SARS-CoV-2 proteins: RBD (kindly provided by Dr. Jens Wrammert, Emory University), S2 extracellular domain (Sino Biologicals) and nucleocapsid (Sino Biologicals) as previously described (Shaan Lakshmanappa et al., 2021). For determination of neutralizing antibody titers, a pseudotype neutralization assays were performed as previously described (Robbiani et al., 2020). The S open-reading frame of the plasmid expressing the SARS-CoV-2 S protein was derived from 'Wuhan seafood market pneumonia virus isolate Wuhan-Hu-1' (GenBank: NC_045512).

In brief, macaque plasma was 4-fold serially diluted and incubated with SARS-CoV-2 pseudotyped HIV-1 reporter virus for 1 hour at 37°C. The plasma/pseudotyped virus mixture was added to HT1080/ACE2.cl14 cells. After 48 hours, cells were washed with PBS, lysed with Luciferase Cell Culture Lysis reagent (Promega) and Nanoluc Luciferase activity in lysates was measured using the Nano-Glo Luciferase Assay System (Promega) and a Glomax Navigator luminometer (Promega). The relative luminescence units were normalized to those derived from cells infected with SARS-CoV-2 pseudotyped virus in the absence of plasma. The half-maximal inhibitory concentrations for plasma (NT_{50}) were determined using 4-parameter nonlinear regression (least-squares regression method without weighting) (GraphPad Prism).

Anti-phospholipid antibody and Anti-nuclear antibody ELISA

Serum Anti-phospholipid antibody (aPL) and Anti-nuclear antibody (ANA) were measured using a competitive ELISA kit (MyBioSource) as per manufacturer's protocol. In brief, phospholipid/Nuclear antigen coated wells were secured in the holder and 100 μL of standard or serum samples were added to the appropriate wells. 100 μL of PBS (pH 7.0-7.2) was added to the blank control well. 50 μL of conjugate was added to each well (NOT blank control well) and the plate was incubated 37°C for 1 hour. Each well was washed five times with 1X wash solution following 1 hour incubation at 37°C. 50 μL of each substrate A and substrate B was added to each well and incubated for 15-20 minutes at 20-25°C. 50 μL of stop solution was added to each well. Optical density (OD) value Absorbance was recorded at 450nm using a Spectramax5 plate reader (Molecular Devices). A standard curve was plotted relating OD value to the concentration of standards. aPL and ANA concentration in each sample was interpolated from this standard curve.

Cell Trace Violet assay

Assessment of proliferating cells by dye dilution was monitored using Cell Trace Violet (CTV) cell proliferation kit (Thermofisher Scientific) (Lakshmanappa et al., 2021). Briefly, the cryopreserved rhesus PBMCs harvested on day −3 and day 7 post infection were washed and re-suspended in 1X phosphate buffered saline (PBS) at a concentration of $1x10^6$ cells/mL. The cells were labeled with CTV at a working concentration of 5 μM for 20 min in a 37°C water bath in the dark. Excess unbound dye was removed after incubating cells with serum free media (SFM) for 5 min. A total of $1x10^6$ CTV-labeled cells were stimulated with a non-human primate CD3/CD28 T cell activation/expansion kit (Miltenyi Biotec) and interleukin IL-2. In parallel, stained unstimulated cells, as well as unstained and stimulated cells, were seeded. To phenotype proliferating cells, cells were stained 5 days post stimulation extracellularly with the following antibody panel: SLAM, CXCR3, CCR6, α4β7, CD69, CD95, CD8, LIVE/DEAD- and intracellularly with CD3 and CD4, after fixation and permeabilization with CYTOFIX/CYTOPERM. Fluorescence was measured on the same day using a BD FACSymphony with FACS Diva version 8.0.1 software.

Mucosal Associated Invariant T cells (MAIT) staining

Phycoerythrin (PE)–conjugated 5-OP-RU–MR1 tetramer or 6-FP (negative control) MR1 tetramer (NIH Tetramer Core Facility, Emory University) was used for the identification of MAIT cells from cryopreserved rhesus PBMCs (harvested on day −3 and day 7), liver and spleen cells (harvested on day 7 post infection). Briefly, cryopreserved rhesus PBMCs/liver/spleen cells were washed and re-suspended in R10 media containing 50nM dasatinib (Sigma Aldrich) at $2x10^7$ cells/mL. Cells were first stained with 5-OP-RU or 6-FP (control) MR1 tetramer at 13ug/mL concentration for 1 hour at room temperature (RT) in the dark before extracellular staining for another 30 min at RT in the dark with the following antibody panel: CD3, CXCR3, PD-1, CD28, CD4, HLA-DR-, CD69, CD95, CD8, and LIVE/DEAD. After washing with 1X phosphate buffered saline (PBS), cells were fixed and permeabilized using Foxp3 Fixation/Permeabilization (F/P) buffer for 20 min at RT in the dark and stained intracellularly in 1X Perm wash buffer for 45 min at 4°C with the following antibody panel: Granzyme B and Perforin. After washing with 1X perm buffer followed by twice washing with 1X FACS buffer, the cells were re-suspended in 200 μL FACS buffer. Fluorescence was measured on the same day on a BD FACSymphony (BD Biosciences) with FACS DIVA v8.0.1 and analyzed with FlowJo software version 10.6.2 (FlowJo LLC).

QUANTIFICATION AND STATISTICAL ANALYSIS

Statistical analysis

R/prcomp function was used to perform a principal components analysis on the given data matrix and ggplot2 (version 3.3.3 package in R). was used to create a plot. The method for calculating the ellipses has been modified from Hayden as described (Hayden, 2012 #68). Statistical analyses were performed using GraphPad Prism 8.4.2. using a Mann-Whitney test. Statistical significance is indicated by the following annotations: *$p < 0.05$, **$p < 0.01$, ***$p < 0.001$, ****$p < 0.0001$.